2024 IEEE/RSJ International Conference on Intelligent Robots and Systems (IROS)
October 14-18, 2024. Abu Dhabi, UAE

Research on Autonomous Navigation of Dual-mode Wheel-legged Robot

Wen Wang[1], Xiaobin Xu[1,*], ZiHeng Chen[1], Jian Yang[2], Yingying Ran[1], Zhiying Tan[1], Minzhou Luo[1]

Abstract— **In order to improve the terrain adaptability and energy efficiency of wheel-legged robot in complex environment, a dual-mode navigation system based on robot energy consumption model is proposed. Firstly, the obstacle trafficability is evaluated according to the maximum obstacle crossing capability of the robot, and the two-dimensional grid map is preprocessed. Secondly, the established energy consumption model is integrated into the evaluation function of A* algorithm, and the eight-adjacency expansion mode is improved to search the surrounding nodes according to the obstacle characteristics of the robot. In the obstacle-crossing area, the obstacle-crossing and obstacle-bypassing modes are intelligently switched based on the principle of minimum energy consumption. Finally, a dual-mode robot navigation system is built, and the experimental results show that the proposed navigation system reduces the average energy consumption, path length, and steering angle by 16.8%, 24.7%, and 31.18%, respectively.**

I. INTRODUCTION

With the rapid advancement of robotics technology, its utilization spans across various fields including military, agriculture, and manufacturing. In these areas, the navigation ability of the robot is the key technology to achieve its autonomous movement and efficient completion of tasks. The traditional single navigation mode struggles in complex and changeable environment. Therefore, by integrating the advantages of different navigation modes and intelligently switching according to the environmental changes can enhance robots' adaptability to various complex scenarios. For instance, Lin [1] employed a behavior pattern manager to intelligently switch between wall-following mode (WFM) and goal-oriented mode (GOM) according to different environmental conditions. This algorithm switches to WFM mode when an obstacle is detected, otherwise it remains in the GOM mode. Literature [2-3] consider that the four-wheeled robot has four independent steering and driving wheels, and can work in a variety of kinematic configurations, such as diagonal moving steering mode, Ackerman mode, sliding mode and point turning mode. Each maneuvering mode features distinct control characteristics and motion advantages, and the maneuverability and applicability of the robot can be improved through multi-mode fusion. Literature [4-5] combine the local tracking control mode in the intelligent switching navigation system of dynamic environment information to improve the real-time performance and smoothness of robot obstacle avoidance.

At present, most of the researches on dual-mode navigation systems for robots focus on how to achieve smooth and safe obstacle avoidance behavior. The research on autonomous navigation with intelligent switching over and around obstacle mode is still in early stages. A few studies on the switching mode of obstacle crossing and obstacle bypassing mainly focus on specific types of robots, such as foot type and wheel-legged type. Literature [6-7] proposed a navigation framework with dual-mode conversion based on the obstacle-crossing characteristics of quadruped robots. The jump mode is selected when the obstacle height is detected and determined to be within the robot's jump capability. Otherwise, the target position is reached in the obstacle bypass mode. Literature [8-9] proposed a learning strategy for wheel-legged robot path planning, which combines reinforcement learning to evaluate the trafficability of obstacles and intelligently switch the mode of crossing and bypassing obstacles. In addition, De [10] proposed a terrain geometry perception module that autonomously selects and adapts the most appropriate crossing behavior. The above multi-mode navigation studies only evaluates whether to switch the obstacle-crossing mode according to the obstacle-crossing ability of the robot. They ignored the adaptability and energy efficiency of robots in complex terrain conditions. This single evaluation mechanism cannot provide the optimal navigation strategy for the robot in the variable and energy-constrained environment. Therefore, this paper proposes a navigation system based on the energy consumption model of wheel-legged robot and the mode switching of obstacle crossing. It aims to provide a more comprehensive and optimized strategy for autonomous navigation of robots in complex and energy-constrained environments by considering factors such as energy consumption, terrain adaptability and navigation efficiency.

In the aspect of robot low energy consumption navigation system, Liu [11] established a robot energy consumption model, incorporating factors such as motor, device, and ground friction. Additionally, they introduced a novel cost function considering energy consumption based on the A* algorithm. However, this algorithm results with excessive redundant turning points along the path and overlooks the corresponding extra energy consumptions. It is reported that a significant amount of energy consumption in robots arises

[1]Wen Wang, Xiaobin Xu, ZiHeng Chen, Yingying Ran, Zhiying Tan, Minzhou Luo are with the College of Mechanical and Electrical Engineering, Hohai University, Changzhou 213200, China. (*Xiaobin Xu is the corresponding author, xxbtc@hhu.edu.cn)

[2]Jian Yang is with the College of Mechanical Engineering, Yangzhou University, Yangzhou 225127, China.

from unnecessary stoppings and turnings [12-15]. The aforementioned low energy navigation systems focus solely on optimizing the robot's motion energy consumption, neglecting comprehensive indicators such as path length and travel time. To address this issue, Chen [16] combined ant colony algorithm with robot energy consumption prediction model to search for the optimal path for robot based on energy consumption, travel time, and travel length. Literature [17-19] use heuristic function based on energy consumption estimation model and distance estimation model to determine the path cost of the A* algorithm. However, the weighting between the two models is not considered, potentially resulting in suboptimal paths. To tackle this issue, Saad [20] proposed a novel composite routing metric algorithm that combines energy consumption model with path length. A composite weight allocation method is used to balance path length and energy consumption. Huang [21] introduced a chaotic-based multi-objective optimizer to determine the optimal weighting between the two indicators. Eder [22] proposed a model based on ResNet neural network architecture using data-driven methods, which can predict energy consumption and traversal time, thus achieving optimal path planning for energy consumption. On this basis, the proposed algorithm comprehensively considers energy consumption factors such as device, friction, direction changing, and obstacle-crossing. To solve the weight assignment problem issues, path length and rotation angles in the evaluation function are transformed into variables with energy attributes based on the robot's dynamics model. By fully leveraging the robot's obstacle-crossing capability mimicking legs, the proposed algorithm minimizes path distance and the number of direction changes while ensuring optimal energy consumption.

The rest of this paper is organized as follows. Section 2 describes the structural design of wheel-legged robot, Section 3 introduces the energy consumption model of wheel-legged robot, Section 4 presents the improved A* algorithm based on energy consumption model and obstacle-crossing mode switching, Section 5 constructs dual-mode navigation system of wheel-legged robot and validates the improved algorithm through simulation and experimentation. Section 6 summarizes the research findings of this paper.

II. Dual-mode Navigation Framework for Robot

The setup of the wheel-legged robot is shown in Fig. 1. The robot consists of a chassis, leg rocker system, track

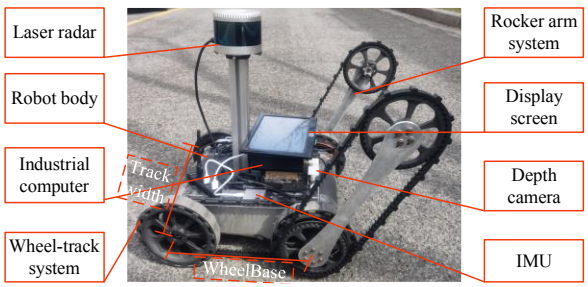

Fig. 1. Physical drawing of wheeled legged robot.

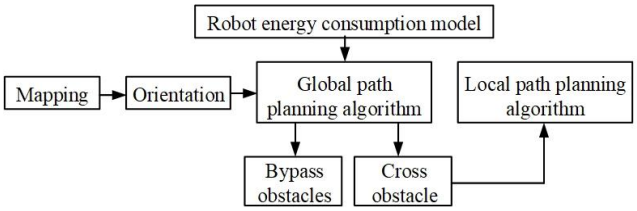

Fig. 2. Dual-mode navigation framework.

system, drive system and external sensor system. The internal and external concentric shaft design is adopted to satisfy the independent driving of the off-road wheel and rocker arm, and four sets of driving equipment are placed on the same axis to reduce the volume of the car body. The center of gravity of the vehicle is set at the front wheel of the vehicle, which is conducive to crossing rugged terrain and obstacles such as gullies and steps.

The dual-mode navigation framework of the robot is shown in Fig. 2. The switching basis of the obstacle crossing and obstacle bypassing modes of the robot is judged according to the combination of energy consumption, distance and steering factors. If the obstacle-crossing mode is adopted, the robot is controlled to cross the obstacle according to the controller proposed in literature [23]. Otherwise, the obstacle is bypassed according to the local planner.

III. Energy Consumption Model

The total energy consumption of wheel-legged robot in the navigation process arises from the devices, friction, directional changes and obstacle-crossing. When the power is turned on, the electronic equipment carried by the robot is in a running state. Assuming that the total device is running at rated power, the equipment energy consumption of the robot E_s is proportional to time t. When the robot moves at a constant speed without steering, the force between the off-road wheel and the ground is rolling friction, and the friction energy consumption E_f is only generated by the work of rolling. When the robot solely performs steering maneuvers, it must overcome both longitudinal friction from wheel rolling and lateral friction from sliding on the ground. Therefore, the pure steering energy consumption of the robot E_b is generated by the work of rolling friction and sliding friction. Combined with the robot kinematics model [23] and literature [24], the sum of the robot's equipment energy consumption, friction energy consumption and pure directional energy consumption can be derived as follows:

$$E_s + E_f + E_b = e_s s + e_\theta \theta_b \tag{1}$$

where e_s and e_θ are respectively:

$$e_s = \frac{e_t}{v} + \frac{30\mu_1 mg}{9.55\pi} \tag{2}$$

$$e_\theta = (\frac{1}{2}\mu_1' \sqrt{d_{wb}^{\ 2} + L_1^{\ 2}} + \frac{15\mu_1 d_{wb}}{9.55\pi})mg + \frac{e_t}{w} \tag{3}$$

where, s is the moving distance, θ_b is the total direction change angle, e_t is the energy consumption rate of the equipment, d_{wb} and L_1 are the wheelbase and track width of the off-road wheel respectively, μ_1 and μ_1' are the rolling friction coefficient and sliding friction coefficient between the off-road wheel and the ground respectively, m is the total mass of the robot, v and w are the robot speed and angular speed respectively.

The wheel-legged robot ascends and descends the obstacle according to the motion planning in literature [25], and the calculation of energy consumption for robot obstacle crossing during this process is relatively complicated. In order to accurately calculate the obstacle crossing energy consumption, dynamic modeling is employed, which convert the electrical energy consumed into several mechanical works.

When the robot crosses an obstacle with height of H, the rocker arm should be rotated clockwise until the crawler wheel is supported on the surface of the obstacle. In this process, the consumed electrical energy is converted into the gravitational potential energy generated by the elevation of the rocker arm and the friction work between the rocker arm and the mechanical parts when it rotates. The sum of the mechanical work done by the robot can be calculated as W_1:

$$W_1 = \tau_a(\pi - \arcsin\frac{H-R+r}{L_1}) \tag{4}$$

where, τ_a is the rotating torque of the rocker arm, R is the radius of the off-road wheel, r is the radius of the track wheel.

Continue to rotate the rocker arm clockwise to rotate the body of the robot around the joint axis at a certain angle under the support of the track wheel. Since the gravitational potential energy consumed by lifting the rocker arm is already included in the mechanical work done by rotating the rocker arm, the following analysis does not calculate the gravity work of rocker arm separately.

Therefore, in this process, the electric energy consumed by the robot is converted into the mechanical work due to the rotation of the rocker arm and the work due to the gravity when the vehicle body is lifted. When the elevation angle of the robot body is α, the total mechanical work W_2 of the robot at this stage is calculated as:

$$\begin{aligned} W_2 = \tau_a(&\arcsin\frac{(1-k_L)(H-R)-k_L r}{k_L L_1} + \arcsin\frac{H-R}{k_L L_1} \\ &+ \arcsin\frac{H-R+r}{L_1}) + m_1 g(L\sin\alpha + h\cos\alpha - h) \end{aligned} \tag{5}$$

where in the vehicle body elevation angle α is expressed as:

$$\alpha = \arcsin((H-R)/k_L L_1) \tag{6}$$

where, L and h are respectively the abscissa and ordinate of the center of mass the robot body, and k_L is the ratio of the intersection of the obstacle horizontal extension line and the body to the total length of the body.

Secondly, the robot moves forward until the vehicle body contacts the obstacle, and the electric energy consumed at this stage is converted into the work done by the rolling friction force between the cross-country wheel and the ground and between the crawler wheel and the obstacle surface. At this time, the stress of the robot is shown in Fig. 3 (a), and the dynamic model of the robot at this time is:

$$\begin{cases} N_1 + N_2 - m_1 g - m_2 g = 0 \\ F_1 + F_2 - f_1 - f_2 = 0 \\ m_1 g(L\cos\alpha - h\sin\alpha) - m_2 g L_1 \cos\alpha + (F_1 - f_1)R - (F_2 \\ -f_2)(H-R) + (N_2 L_1 + m_2 g)(\cos\alpha - \cos(\alpha - \arcsin(((1 \\ -k_L)(H-R) - k_L r)/k_L L_1) + \arcsin((H-R)/k_L L_1))) = 0 \end{cases} \tag{7}$$

where, γ is the angle between the center line of the crawler wheel and the horizontal line, m_1 and m_2 are the mass of the vehicle body and the rocker arm respectively, N_1 is the sum of the equivalent supporting forces of the ground on the two rear cross-country wheels, N_2 is the sum of the equivalent supporting forces of the obstacle on the two crawler wheels, and f_1 is the sum of the rolling friction forces between the two rear cross-country wheels and the ground, f_2 is the sum of the rolling friction forces between the obstacle and the two track wheels, μ_2 is the coefficient of rolling friction between the track wheels and the surface of the obstacle, F_1 and F_2 are the driving forces of the robot to the cross-country wheel and the track wheels respectively, and $M_1=F_1R+F_2r$.

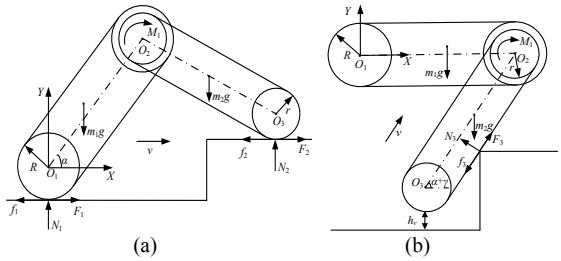

Fig. 3. Obstacle crossing dynamics model: (a)state 1; (b) state 2;

In order to simplify the calculation, it is assumed that the track wheel and the cross-country wheel are made of the same material and the roughnesses of the obstacle surface and the ground are the same, that is, the rolling friction coefficient $\mu_2=\mu_1$. Then the mechanical work W_3 caused by the friction force when the robot moves forward is:

$$\begin{aligned} W_3 = \mu_1 m g L_1((1-k_L)\cos\alpha - k_L R/(H-R) \\ + \cos(\arcsin((1-k_L)(H-R) - k_L r)/(k_L L_1))) \end{aligned} \tag{8}$$

Then, the rocker arm is rotated counterclockwise to make the robot lift the body under the support of the crawler wheel, and the electric energy consumed in this process is the sum of the mechanical work done by the rocker arm rotation and the lifting of the body. When the lifting angle of the vehicle body is θ_1, the total mechanical work W_4 done by the robot at this stage is calculated as:

$$W_4 = \tau_a(\arcsin\frac{(1-k_L)(H-R)-k_L r}{k_L L_1} + \arcsin\frac{H-R}{k_L L_1} + \theta_1 + \gamma + \pi) + m_1 gh(\cos(\theta_1-\alpha-\gamma)-\cos\alpha) + m_1 gL(\sin(\theta_1-\alpha-\gamma) + m_1 g\sin(\alpha+\gamma)) \quad (9)$$

Finally, the robot ascends the obstacle under the action of the driving force, and resets the rocker arm after successfully crossing the obstacle. When the height of the robot above the ground is h_v, the force condition is shown in Fig. 3 (b). According to the force analysis, the dynamic model of the robot climbing the obstacle is established as follows:

$$\begin{cases} N_3\cos(\alpha+\gamma)+(F_3-f_3)\sin(\alpha+\gamma)-m_1 g-m_2 g=0 \\ F_3\cos(\alpha+\gamma)-N_3\sin(\alpha+\gamma)=0 \\ -m_2 g(L_1-L_2\cos(\alpha+\gamma))+((F_3-f_3)\sin(\alpha+\gamma)+N_3\cos(\alpha \\ +\gamma))(L_1-L_1\cos(\alpha+\gamma)+(H-h_v)/\tan(\alpha+\gamma))-m_1 gL=0 \end{cases} \quad (10)$$

where N_3 is the equivalent supporting force of the obstacle to the track, f_3 is the friction force between the obstacle and the track, μ_3 is the sliding friction coefficient between the obstacle and the track, F_3 is the driving force of the robot to the track, and $M_1=F_3 r$.

The electric energy consumed by the robot is the sum of the mechanical work done by the gravity of the vehicle body, the friction force f_3 between the obstacle and the track, and the reset of the rocker arm, the sum of the mechanical work W_5 can be calculated as follows:

$$W_5 = \tau_a(\theta_1+\gamma) + m_1 g(L(\sin\theta_1-\sin\alpha-\sin(\theta_1-\alpha-\gamma) - \sin(\alpha+\gamma)) + h(\cos\theta_1-\cos(\theta_1-\alpha-\gamma)) + H) + f_3(L_1-((1-k_L)L_1\sin\alpha - r\cos(\alpha+\gamma))/\sin(\alpha+\gamma)) \quad (11)$$

When the robot descends the obstacle, the energy consumption analysis process is the same as the analysis method when the robot ascends. First, rotate the rocker arm clockwise until it touches the ground, the work done by the robot is $W_6=\tau_a(\pi+\arcsin((H+R-r)/L_1))$. Then the robot moves forward for a certain distance until the rear cross-country wheel reaches the boundary of the obstacle, and the consumed electric energy at this stage is the sum of the work done by the friction force between the rear cross-country wheel and the obstacle and the friction force between the crawler wheel and the ground. Since the rolling friction coefficient between the cross-country wheel or the crawler wheel and the ground or the obstacle is the same, the dynamic model of the robot at this time is similar to that shown in Fig. 3 (a), so the mechanical work done by the robot at this stage is $W_7=\mu_1 mgL_1$.

Secondly, rotate the rocker arm counterclockwise to make the body lift at an angle of θ_1', then the sum W_8 of the mechanical work done by the robot rotating the rocker arm and the work done by the robot gravity at this stage is:

$$W_8 = \tau_a(\pi+\arcsin\frac{H+R-r}{L_1}+\arcsin\frac{R-r}{L_1}+\theta_1') + h(\cos(\theta_1'-\arcsin(\frac{H-R+r}{L_1}))-\cos(\arcsin(\frac{H-R+r}{L_1})) + m_1 g(L(\sin(\theta_1'-\arcsin(\frac{H-R+r}{L_1}))+\frac{H-R+r}{L_1}) \quad (12)$$

Finally, the robot moves forward for a certain distance and lands successfully, and the rocker rotates clockwise to reset, so the total mechanical work W_9 in this process is:

$$W_9 = \tau_a(\theta_1'+\arcsin\frac{R-r}{L_1}) + \mu_1 mgR \quad (13)$$

IV. NAVIGATION ALGORITHM

This article constructs a 2D grid map by reducing the dimensionality of point cloud data acquired from 3D LiDAR. Considering the obstacle-crossing capability of wheel-legged robots, we assessed obstacle accessibility according to the robot's maximum obstacle-crossing performance. The occupied area was divided into accessible and inaccessible regions using the obstacle height H_{max} as the evaluation criterion. Hence, we divide the grid state into four categories: free, accessible, inaccessible, and unknown. The grayscale value range of the accessible area is set to be 213 to 244. When the height of the obstacle in the accessible area is H, the grayscale value function of the accessible area $G(H)$=244-[H/5]. Prepare the 2D grid map for global planning by preprocessing it based on the grayscale value information derived from the accessible area.

In order to achieve the goal of low energy path search, we integrate the robot energy consumption model into the cost function of path planning on the basis of the traditional A* algorithm. In complex environments, when the robot encounters obstacles within the accessible area, intelligent mode switches based on the comparison between the energy consumption of crossing the obstacle and that of bypassing it. This facilitates meeting the path planning requirements of the robot.

Integrating the robot energy consumption model into the cost function of the A* algorithm yields an improved cost function as:

$$F(n) = e_s g(n) + e_\theta \theta_b + E_o + e_s h(n) \quad (14)$$

Based on the state of the current node n and the extended node, the energy consumed by the robot's autonomous obstacle crossing E_o can be categorized into three scenarios: if the current node belongs to the free zone and the extended node belongs to the accessible zone, then $E_o=E_{up}$; If the current node belongs to the accessible zone and the extended node belongs to the free zone, then $E_o=E_{down}$; If both the current node and the extension node belong to the free zone or accessible zone, then E_o=0.

When expanding from the current node to neighboring child nodes, enhance the eight-adjacency extension method by

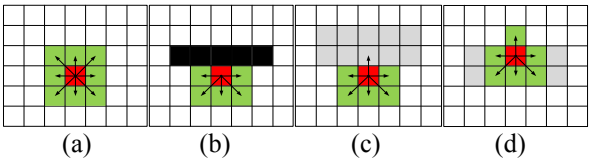

Fig. 4. Improved adjacency mode of A* algorithm: (a)free zone; (b) do not cross obstacle zone; (c) up steps; (d) down steps;

integrating the robot's obstacle-crossing characteristics. When in the above situation 3), the selection method of child nodes is the same as the traditional A* algorithm, as shown in Fig. 4 (a). When the current node belongs to the free zone and the extended node belongs to the inaccessible zone, skip this node, as shown in Fig. 4 (b). When in situations 1) and 2) above, both the upper and lower obstacle of the robot are required to execute obstacle-crossing actions in a direction perpendicular to the obstacle. At this time, only the extension nodes perpendicular to the direction of obstacle placement are retained, as shown in Fig. 4 (c) and Fig. 4 (d). Furthermore, assign key point attributes indicating climbing up or down obstacle to the current node.

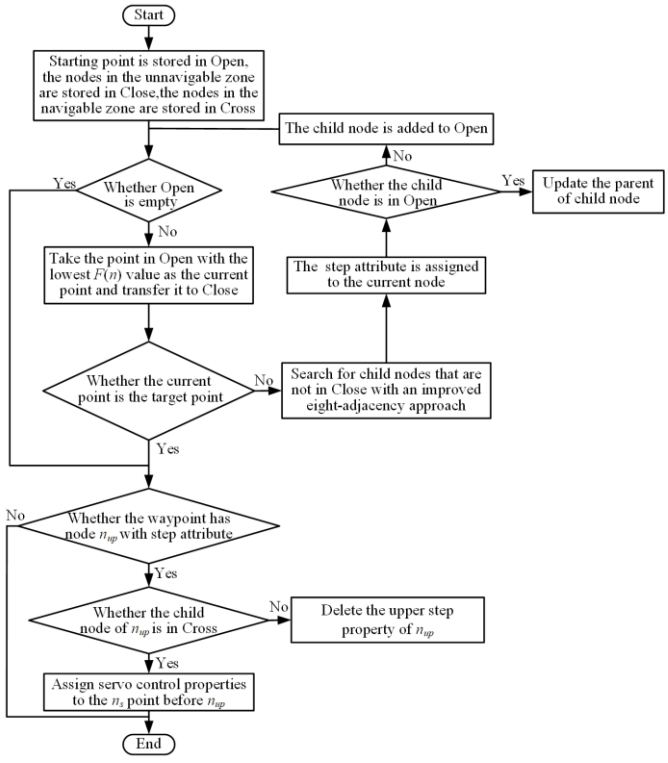

Fig. 5. Improved A* algorithm flowchart.

If there is a node n_{up} with the attribute of climbing obstacles in the node generated by the robot, determine whether the next node of this node belongs to accessible zone. If not, the algorithm chooses the obstacle avoidance mode and remove the attribute of climbing obstacles of the node n_{up}. If the next node belongs to the accessible zone, the algorithm selects the accessible mode. Due to the need for pose adjustment before the robot crosses obstacles, visual servo control attributes are assigned to the $n_s th$ node in front of the node n_{up}. Based on the map resolution D', n_s is defined as:

$$n_s = \begin{cases} n_{up} - 1/D' & n_{up} \geq 1/D' \\ 0 & n_{up} < 1/D' \end{cases} \tag{15}$$

The process of the improved A* algorithm incorporating energy consumption model and obstacle crossing mode switching is shown in Fig. 5. The specific implementation steps are as follows:

Step 1: Set the starting and destination points of the path, initialize three empty lists: Open table, Close table, and Cross table. The Cross table is used to store the node information of the accessible area, the height of obstacles in that area, and the placement direction. Store the starting point in the Open table, store nodes of inaccessible zone in the Close table, and store node information that can be crossed in the Cross table.

Step 2: Check if there are any undetected nodes in the Open table. If the Open table is empty, proceed to step 5. If the Open table is not empty, traverse the nodes in the Open table and select the node with the lowest *F(n)* value as the current node. Mark the current node as a detected node in the Open table and store it in the Close table.

Step 3: Determine if the current node is the target point. If it is, proceed to step 5. If it is not the target point, expand the neighborhood nodes based on the improved eight adjacency method, and determine whether to assign key point attributes indicating climbing up or down obstacle to the current node.

Step 4: Determine whether the extension node is in the Open table. If it is, compare the *F(n)* value. If the total proxy value is smaller than the original total proxy value, update the parent node and total proxy value; If not present, store this node in the Open table. Then go to step two.

Step 5: Starting from the target point, sequentially retrieve the nodes from the Close table through backtracking, and output the global optimal path from the starting point to the target point. Determine whether the output path is in obstacle avoidance mode or obstacle crossing mode. If it is in obstacle crossing mode, assign visual servo control attributes to the n_s node before n_{up}, and the algorithm ends.

V. EXPERIMENT

To verify the accuracy of the energy consumption model of the wheel-legged robot, experiments were conducted on four scenarios: the robot walked straight for 1 meter, turn in place for two laps, and autonomously ascending and descending. The theoretical and measured values of the robot's energy consumption will be compared. In order to obtain accurate and real-time values, we have installed voltage and current sensors on the robot body, which can collect current and voltage data of each motor and upload it to the computer in real time through serial communication. At this

time, we can obtain the actual energy consumption. By substituting the structural parameters of the robot in Table 1 into the energy consumption formula to obtain the theoretical energy consumption value of the robot. The step height in the experiment was set to 0.15m. Table 2 presents the measured energy consumption statistics and theoretical energy consumption calculation data of the robot in four different scenarios. As shown in the table, when the robot travels straight on flat ground for 1 meter and turns in place for two laps, the energy consumption deviations are only 4.87 J and 11.77 J, respectively. It indicates that the flat friction energy consumption model and the directional energy consumption model are consistent with reality, with relatively small errors. When the robot ascends and descends, the energy consumption deviations are 27.48J and 20.45J, respectively. This deviation stems from the average energy consumption time in the energy consumption model for the robot's going up and down. In reality, the robot's crossing time varies with the height of the obstacles, leading to fluctuations in equipment energy consumption. This deviation falls within the allowable error range in the global path planning of robots. Therefore, the theoretical energy consumption model of robots derived in this article is proven to be accurate and feasible.

TABLE I. PARAMETERS OF WHEEL-LEGGED ROBOT

Name	Value	Name	Value
Off road wheel track width d_{wb}	300 mm	Frictional coefficient μ_1	0.27
Off road wheel center distance L_1	71.75 mm	Frictional coefficient μ_1'	0.35
center of mass (L, h)	(150 mm,30 mm)	Frictional coefficient μ_3	0.42
Track wheel radius r	71.75 mm	Scale k_L	0.33
Off road wheel radius R	86.5 mm	Equipment energy consumption rate e_t	34 J/s
Rocker arm mass m_2	0.189 kg	Angle θ_1'	0.17 rad
Vehicle mass m_1	11.48 kg	Torque τ_a	24 N·m
angular velocity w	0.97 rad/s	Angle γ	0.039 rad
velocity v	0.28 m/s	Angle θ_1	1.16 rad

TABLE II. COMPARISON OF THEORETICAL ENERGY CONSUMPTION ENERGY CONSUMPTION OF ROBOT

Scenarios	Theoretical energy consumption /J	Actual energy consumption /J	Energy consumption deviation /J
Go straight for 1 meter	208.06	212.93	4.87
Spin around 2 laps	2595.12	2606.89	11.77
Upper obstacle	804.75	832.23	27.48
Descending obstacle	383.13	403.58	20.45

To assess the effectiveness of dual-mode navigation, an indoor simulation scenario was initially established, as shown in Fig. 6 (a). Firstly, the robot employs LeGO-LOAM algorithm to construct a 3D point cloud map of the environment. Next, NDT positioning algorithm aligns the map with LIDAR data to furnish global positioning information for the robot. Fig. 6 (b) illustrates the positioning effect. Secondly, utilizing point cloud filtering and projection techniques, the 3D point cloud map is converted into a 2D grid map. Subsequently, the accessible areas within 2D grid map are segmented based on map preprocessing methodology. The preprocessed 2D map is depicted in Fig. 6 (c).

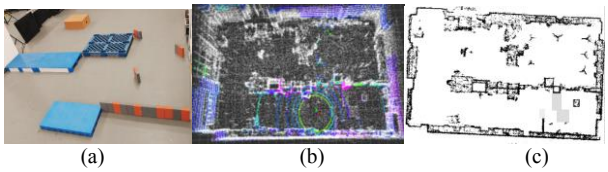

(a) (b) (c)

Fig. 6. Indoor simulation scene; (b) 3D positioning effect; (c) pre-processed 2D raster map;

When the starting and target points of the robot are set to (0, 0) and (6.49, -0.51), the path effects planned by the two algorithms are shown in Fig. 7. In terms of path length, A* algorithm planned a path length of 8.10 m, while the improved algorithm planned a path length of 7.92 m. Because the improved algorithm opted for obstacle avoidance mode when encountering three accessible zones, resulting in a slight disparity in path length between the two scenarios, with only a 2.22% reduction observed. In terms of total turning angle, A* algorithm is 630°, while the improved algorithm is merely 315°, reducing by 50%. Moreover, the path planned by A* algorithm is close to the edge of the obstacle, resulting in poor path smoothness and low safety. In terms of energy consumption, A* algorithm consumes 4505.5J along the path, while the consumption of improved algorithm is 3326.67J, reducing by 26.7%.

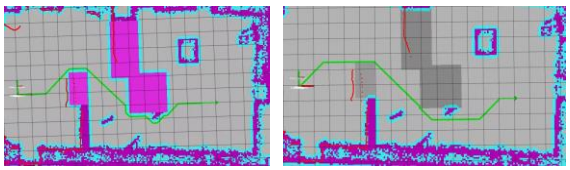

(a) (b)

Fig. 7. Paths planned by different algorithms: (a) A* algorithm;.(b) improved A* algorithm;

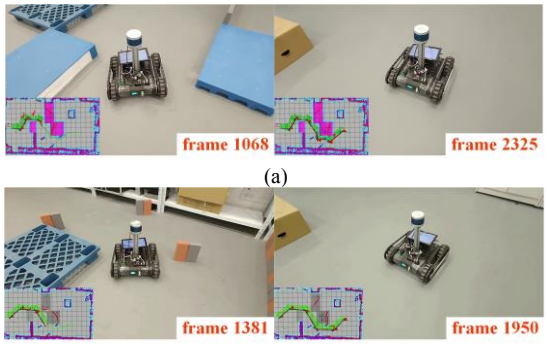

(a)

(b)

Fig. 8. Trajectories of different navigation systems: (a) single-mode navigation systems; (b) dual-mode navigation system;

Fig. 8 shows the motion process of the robot under the conventional single-mode navigation system and the dual-mode navigation system. The evaluation data presented in Table 3 indicate that compared to single-mode navigation system, the dual-mode navigation system has reduced the path length by 16.41%, decreased the steering angle by 25%, and lowered actual motion energy consumption by 19.14%.

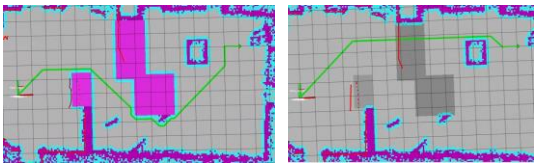

(b) (b)

Fig. 9. Paths planned by different algorithms: (a) A* algorithm; (b) improved A* algorithm;

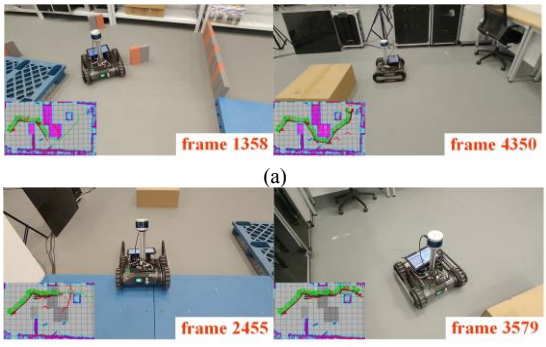

(a)

(b)

Fig. 10. Trajectories of different navigation systems: (a) single-mode navigation systems; (b) dual-mode navigation system;

When the starting point and target point of the robot are set to (0,0) and (7.98,1.51), respectively, the path effects planned by the two algorithms are shown in Fig. 9. The path length planned by A* algorithm is 10.3 m, the total turning angle is 585°, and the theoretical motion energy consumption is 5005.37J. In contrast to A* algorithms, the improved algorithm adopts the obstacle-crossing mode based on the principle of optimal energy consumption when encountering the second obstacle zone, particularly when the target point is situated farther from the obstacle's edge. Consequently, the planned path length is reduced to 7.98 m, marking a 22.52% decrease compared to A* algorithms. Furthermore, the total turning angle is merely 180°, reflecting a substantial 69.23% reduction compared to A* algorithms. The calculated motion energy consumption is 3511.09 J, indicating a notable 29.85% decrease compared to A* algorithms. When the improved algorithm selects the obstacle avoidance mode, the robot shows significant improvements in energy consumption, steering angle, and path length. In terms of time efficiency, by switching modes to obstacle crossing, the running time has increased by 17.82%, greatly improving efficiency.

Fig. 10 shows the motion process of the robot under the conventional single-mode navigation system and dual-mode navigation system. As shown in Fig. 10(a), the actual number of turning points in the robot's path under the traditional navigation system is excessive, which affects the stability and safety of the robot's motion process. Fig. 10 (b) shows the actual movement process of the robot under the dual-mode navigation system. Based on the evaluation data of the second set of experiments in Table 3, it can be seen that the dual-mode navigation system has shortened the path length by 36.51%, reduced the total turning angle by 37.62%, and reduced actual motion energy consumption of robot by 19.7%.

In addition to the two sets of comparative experiments mentioned above, we also set multiple different initial and target points to comprehensively evaluate the performance of the dual-mode navigation system in indoor simulation scenarios. The experimental results are shown in Table 3. The dual-mode navigation system shows significant advantages in multiple evaluation indicators on average, energy consumption decreased by 16.8%, path length decreased by 24.7%, and steering angle decreased by 31.18%. Our algorithm reduces unnecessary detours and turns while optimizing the energy consumption of robot motion.

VI. Conclusion

To improve the energy efficiency during robot navigation, this paper proposes a dual-mode wheel-legged robot autonomous navigation system. Firstly, the energy consumption during robot motion is analyzed, and considering the robot's dynamic model, energy consumption models for flat terrain motion and obstacle-crossing motion are established. Then, considering the robot's maximum

TABLE III. Comparison of Navigation Performance of Different Path Planning Algorithms in Indoor Simulation Environmen

Group	Start Point /m	Target point /m	Navigation system	Energy consumption /J	Distance /m	Angle /°	Running time/s	Model
1	(0,0)	(6.49,-0.51)	Single-mode navigation	5500.72	10.36	360	62.97	\
			Dual-mode navigation	4448.6	8.66	270	53.32	Bypass obstacle
2	(0,0)	(7.98,1.51)	Single-mode navigation	7237.72	12.68	505	75.16	\
			Dual-mode navigation	5811.79	8.05	315	61.77	Obstacle crossing
3	(0.46,0.93)	(5,2)	Single-mode navigation	6148.53	11.79	455	48.54	\
			Dual mode navigation	4854.3	5.08	225	37.23	Obstacle crossing
4	(1.57,1.59)	(4.42,-1.36)	Single-mode navigation	4541.6	6.79	305	46.62	\
			Dual-mode navigation	3604.34	5.32	235	39.15	Bypass obstacle
5	(2.64,1.28)	(7.01,0.26)	Single-mode navigation	5331.43	9.65	355	59.29	\
			Dual-mode navigation	5147.23	4.93	285	44.81	Obstacle crossing

obstacle-crossing capability, the 2D map is preprocessed with traversability analysis. Finally, for traversable regions, an improved A* algorithm is developed upon the robot's energy consumption model. The algorithm intelligently switches between obstacle-crossing and obstacle-bypassing modes, enabling the robot to achieve the shortest path length while minimizing energy consumption. The main contributions are:

(1) This paper comprehensively considers factors affecting robot motion energy cost and establishes the energy consumption model. Experimental result indicates a mere 2.79% variance between the theoretical and the measured energy consumptions of the robot.

(2) A dual-mode navigation system for wheel-legged robot is built by improved A* algorithm. The experimental results demonstrate significant advantages over the single-mode navigation system, in terms of robot motion energy consumption, path length, and number of turnings. The dual-mode navigation system reduces the average energy consumption, path length, and turning angle by 16.8%, 24.7%, and 31.18%, respectively.

REFERENCES

[1] C. H. Lin, S. H. Wang, and C. J. Lin, "Interval type-2 neural fuzzy controller-based navigation of cooperative load-carrying mobile robots in unknown environments," *Sensors*, vol. 18, no. 12, Dec. 2018.

[2] Y. L. Xie, X. L. Zhang, W. Meng, S. N. Xie, L. Q. Jiang, J. Meng, and S. T. Wang, "Coupled sliding mode control of an omnidirectional mobile robot with variable modes," In Proceedings of 2020 In *IEEE/ASME International Conference on Advanced Intelligent Mechatronics (AIM)*. IEEE, 2020, pp. 1792–1797.

[3] J. Ni, J. B. Hu, and C. L. Xiang, "Robust control in diagonal move steer mode and experiment on an X-by-wire UGV," *IEEE/ASME Transactions on Mechatronics*, vol. 24, no. 2, pp. 572–584, APR 2019.

[4] Q. L. Li, X. Liu, S. H. Wang, Y. R. Luo, H. S. Hong, and Y. X. Zhang, "Obstacle Avoidance System of Substation Inspection Robot Based on the Dual-mode Controller of Bumpless Switching," In *2019 4th International Conference on Communication and Information Systems (ICCIS)*. IEEE, 2019.

[5] S. Berkane, A. Bisoffi, and D. V. Dimarogonas, "Obstacle avoidance via hybrid feedback," *IEEE Transactions on Automatic Control*, vol. 67, no. 1, pp. 512-519, Jan. 2021.

[6] S. Gilroy, D. Lau, L. Z. Yang, E. Izaguirre, K. Biermayer, A. X. Xiao, M. T. Sun, A. Agrawal, J. Zeng, Z. Y. Li, and K. Sreenath, "Autonomous navigation for quadrupedal robots with optimized jumping through constrained obstacles," In *2021 IEEE 17th International Conference on Automation Science and Engineering (CASE)*. IEEE, 2021, pp. 2132-2139.

[7] X. L. Zhang, Y. Huang, S. T. Wang, W. Meng, G. Li, and Y. L. Xie, "Motion planning and tracking control of a four-wheel independently driven steered mobile robot with multiple maneuvering modes," *Frontiers of Mechanical Engineering*, vol. 16, no. 3, pp. 504–527, Sep 2021.

[8] J. Li, H. Qin, J. Z. Wang, and J. H. Li, "Openstreetmap-based autonomous navigation for the four wheel-legged robot via 3d-lidar and ccd camera," *IEEE Transactions on Industrial Electronics*, vol. 69, no. 3, pp. 2708-2717, Apr. 2021.

[9] V. S. Raghavan, D. Kanoulas, D. G. Caldwell, and N. G. Tsagarakis, "Reconfigurable and agile legged-wheeled robot navigation in cluttered environments with movable obstacles," *IEEE Access*, vol. 10, pp. 2429-2445, 2021.

[10] De Luca, Alessio, Muratore, Luca, Raghavan, Vignesh Sushrutha, Antonucci, Davide and Tsagarakis Nikolaos G. "Autonomous obstacle crossing strategies for the hybrid wheeled-legged robot centauro." *Frontiers in Robotics and AI,* vol.8, pp.721001, 2021.

[11] S. Liu and D. Sun, "Minimizing energy consumption of wheeled mobile robots via optimal motion planning," *IEEE Transactions on Mechatronics*, vol. 19, no. 2, pp. 401–411, Feb. 2013.

[12] A. Pal, R. Tiwari, and A. Shukla, "Modified A* algorithm for mobile robot path planning," *Soft computing techniques in vision science*, 2012, pp. 183-193.

[13] R. Kurazume, A. Byong-Won, K. Ohta, and T. Hasegawa, "Experimental study on energy efficiency for quadruped walking vehicles," In *Proceedings 2003 IEEE/RSJ International Conference on Intelligent Robots and Systems (IROS 2003)*. IEEE, 2003, pp. 613-618.

[14] Hsu PM, Lin CL, and Yang MY, "On the complete coverage path planning for mobile robots," *Journal of Intelligent & Robotic Systems*, vol. 74, pp. 945-963, Jun. 2014.

[15] T. Liu, J. M. Li, S. X. Yang, Z. D. Gong, Z. L. Liu, H. Zhong, and Q. Fu, "optimal coverage path planning for tractors in hilly areas based on energy consumption model," *International Journal of Robotics & Automation*, vol. 38, no. 1, pp. 20–31, Jul. 2023.

[16] J. Chen, F. Ling, Y. Zhang, T. You, Y. Liu, and X. Du, "Coverage path planning of heterogeneous unmanned aerial vehicles based on ant colony system," *Swarm and Evolutionary Computation*. vol. 69, Mar. 2022.

[17] K. Zakharov, A. Saveliev, and O. Sivchenko, "Energy-efficient path planning algorithm on three-dimensional large-scale terrain maps for mobile robots," *Interactive Collaborative Robotics: 5th International Conferenc*e, ICR 2020, pp. 319-330.

[18] H. Kim, and B. K. Kim, "Online minimum-energy trajectory planning and control on a straight-line path for three-wheeled omnidirectional mobile robots," *IEEE Transactions on industrial electronics*, vol. 61, no. 9, pp. 4771-4779, Dec. 2013.

[19] B. Guo, Z. Kuang, J. H. Guan, M. T. Hu, L. X. Rao, and X. Q. Sun, "An improved a-star algorithm for complete coverage path planning of unmanned ships," *International Journal of Pattern Recognition and Artificial Intelligence*, vol. 36, no. 03, Mar. 2022.

[20] M. Saad, A. I. Salameh, and S. Abdallah, "Energy-efficient shortest path planning on uneven terrains: A composite routing metric approach," *in 2019 IEEE International Symposium on Signal Processing and Information Technology (ISSPIT)*. IEEE, 2019, pp. 1-6.

[21] G. M. Huang, X. F. Yuan, K. Shi, Z. X. Liu, and X. R. Wu, "A 3-d multi-object path planning method for electric vehicle considering the energy consumption and distance," *IEEE Transactions on Intelligent Transportation Systems*, vol. 23, no. 7, pp. 7508-7520, Apr. 2021.

[22] M. Eder and G. Steinbauer-Wagner, "Predicting Energy Consumption and Traversal Time of Ground Robots for Outdoor Navigation on Multiple Types of Terrain", In *Proceedings 2023 IEEE/RSJ International Conference on Intelligent Robots and Systems (IROS 2023)*. IEEE, 2023, pp. 8104-8111.

[23] W. Wang, X. B. Xu, Z. H. Chen, Z. Q. Zhang, H. J. Zhang, and Z. Y. Tan, "Visual Servoing Control Method of 3D Robot Based on 3D Point Cloud Processing," *In Proceedings of the 2023 3rd International Conference on Robotics and Control Engineering*, 2023, pp. 209-214.

[24] C. Liu, X. B. Xu, X. H. Li, Z. J. Pan, K. Hu, and Y. Shu, "Path Planning for an Omnidirectional Mobile Robot Based on Modified A* Algorithm with Energy Model," In *2021 IEEE International Conference on Progress in Informatics and Computing (PIC)*. IEEE, 2021, pp. 462-468.

[25] X. B. Xu, W. Wang, G. Y. Su, C. Liu, W. Cai, H. J. Zhang, Y. Y. Ran, Z. Y. Tan, and M. Z. Luo, "Obstacle Modeling and Structural Optimization of Four-Track Twin-Rocker Rescue Robot," *Machines*, vol. 10, no. 5, May. 2022.